Deep-Sea Research I 58 (2011) 429–441

Contents lists available at ScienceDirect

Deep-Sea Research I

journal homepage: www.elsevier.com/locate/dsri

Inter-annual variations in the SeaWiFS global chlorophyll *a* concentration (1997–2007)

V. Vantrepotte [a,*], F. Mélin [b]

[a] Laboratoire d'Océanologie et de Géosciences, UMR CNRS 8187 LOG-ULCO-Univ. Lille Nord de France, F-62930, Wimereux, France
[b] European Commission - Joint Research Centre, Institute for Environment and Sustainability, Global Environment Monitoring Unit, TP272, ISPRA 21027, Italy

ARTICLE INFO

Article history:
Received 27 May 2010
Received in revised form
3 February 2011
Accepted 7 February 2011
Available online 12 February 2011

Keywords:
Chlorophyll
Time series
Global
Census X-11
Climate
Trends

ABSTRACT

The SeaWiFS data set covering the period 1997–2007 is used to develop a framework for a comprehensive description of the inter-annual variations in chlorophyll *a* concentration (Chl*a*). For each grid cell, the monthly Chl*a* series is decomposed into seasonal, irregular and trend-cycle terms with the Census X-11 technique that is an iterative band-pass filter algorithm. This approach allows variations in the annual cycle, while the trend-term isolates the multi-annual evolution in the mean level of the signal. The patterns with relatively large inter-annual variations are selected using the variance due to the trend-term with respect to the total variance, and are compared with maps of monotonic trends derived by a non-parametric Kendall analysis. Most of these patterns are identified in the subtropical domain (30°S–30°N), even though there are patterns with strong variations at mid-latitudes, particularly in the Northeast Atlantic and South of Australia. The time series found within each pattern of interest are found coherent. Conversely, the ensemble of spatially averaged time series of Chl*a* trend-terms shows a diversity of evolutions, with rather monotonic changes for all or part of the period, abrupt shifts or low-frequency oscillations, sometimes coupled with a modification in the amplitude of the annual cycle. Some of these series are correlated with climate indices, and those in subtropical regions usually show a negative correlation with the equivalent trend-term calculated for sea surface temperature. The identified inter-annual signals should be further monitored with longer time series and can serve as test cases for biogeochemical models.

1. Introduction

The sensitivity of the algal communities to the physical environment (temperature, stratification, wind regime, sea ice cover) is expressed across a range of space and time scales (Mann and Lazier, 1996), and long-term climate changes are expected to affect marine phytoplankton in terms of biomass and species composition for entire ocean regions (e.g., Sarmiento et al., 2004; Bopp et al., 2005). The assessment of inter-annual changes in phytoplankton populations and the understanding of the climate effects on ocean biology requires appropriately long data series. In that respect, satellite ocean color is a precious asset since it now provides a synoptic view of the phytoplankton biomass distribution for an extended period. Specifically, the global coverage provided by the Sea-viewing Wide Field-of-view Sensor (SeaWiFS) offers a 10-year time series of consistent, well calibrated, data record of chlorophyll *a* concentration (Chl*a*) that is particularly suitable for temporal analysis (McClain et al., 2004a). Significant changes in the level of phytoplankton Chl*a* in response to long-term climate changes have already been illustrated at global scale by previous works using the SeaWiFS data record and regression analysis (McClain et al., 2004b; Gregg et al., 2005; Behrenfeld et al., 2006; Polovina et al., 2008; Irwin and Oliver, 2009). However, more complex variations like abrupt non-linear changes may affect marine ecosystems (Stenseth et al., 2002; Hsieh et al., 2005; Kirby and Beaugrand, 2009), and oscillations or regime shifts have been detected at basin scales, in the Pacific (e.g., Karl et al., 2001; Chavez et al., 2003) or the Atlantic (e.g., Beaugrand and Reid, 2003). Data series need to be analyzed in this context.

The first aim of this study is to identify at global scale the major inter-annual patterns in the Chl*a* record over the 10-year SeaWiFS period. The second objective is to describe their main temporal evolution with a much greater level of detail than currently documented. Practically, two statistical approaches are considered. Firstly, the presence of significant monotonic trends in the Chl*a* signal is examined by classical non-parametric statistics. In addition, Chl*a* monthly time series are broken down into seasonal, irregular and trend components using the Census

* Corresponding author.
E-mail addresses: vincent_vantrepotte@yahoo.fr, vincent.vantrepotte@univ-littoral.fr (V. Vantrepotte), frederic.melin@jrc.ec.europa.eu (F. Mélin).

0967-0637/$ - see front matter © 2011 Elsevier Ltd. All rights reserved.
doi:10.1016/j.dsr.2011.02.003

Table 1
Climate indices provided for the various ocean basins. The column data refers to the data used to derive the index. The MEI uses sea surface temperatures, surface air temperatures, sea-level pressure, zonal (i.e., east–west) surface wind, meridional (i.e., north–south) surface wind and total amount of cloudiness. Data sources are reported below the corresponding indices.

Name (acronym)	Location	Data	Reference
Multivariate ENSO Index (MEI) *Source*: http://www.esrl.noaa.gov/psd/people/klaus.wolter/MEI/mei.html	Tropical Pacific	Cf. legend	Wolter and Timlin (1998)
Pacific Decadal Oscillation (PDO) *Source*: http://jisao.washington.edu/pdo/	$>20^{\circ}$N	SST	Mantua et al. (1997)
North Atlantic Oscillation (NAO) *Source*: http://www.cgd.ucar.edu/cas/jhurrell/indices.html	North Atlantic	Atm. pressure	Hurrell (1995)
Tropical Northern Atlantic (TNA)	55°W–15°W, 5°N–25°N	SST	Enfield et al. (1999)
Tropical Southern Atlantic (TSA)	30°W–10°E, 20°S–0°	SST	Enfield et al. (1999)
Niño 1+2	90°W–80°W, 10°S–0°	SST	Rayner et al. (2003)
Niño 4	160°E–150°W, 5°S–5°N	SST	Rayner et al. (2003)
Indian Ocean Dipole Mode Index (DMI) *Source*: http://ioc3.unesco.org/oopc/state_of_the_ocean/sur/	E-W gradient	SST	Saji et al. (1999)
Southern Annular Mode (SAM) *Source*: http://www.nerc-bas.ac.uk/icd/gjma/sam.html	40°S–65°S	Atm. pressure	Marshall (2003)

X-11 decomposition method. This approach allows year-to-year changes in the shape of the annual cycle, thus providing information on the inter-annual variations of this part of the signal. Consequently, the X-11 trend-term is not affected by inter-annual changes in seasonality and is well adapted to describe the non-linear multi-annual changes in the series (Pezzulli et al., 2005). The study first presents these statistical approaches and then the results for the global ocean. Specific patterns with a relevant inter-annual variability are selected using the relative contribution of the X-11 trend-term to the total variance and are described using the outputs of the two complementary temporal analyzes. Even though investigating the factors driving these patterns is not an objective of the present work, some trend patterns are discussed with respect to temperature and climate variations.

2. Material and methods

2.1. Satellite data

The satellite product is the concentration of Chl*a* in the upper layer of the ocean derived from the SeaWiFS sensor and associated algorithms (reprocessing R2009[1]), and obtained as Level-3 monthly files from the U.S. National Aeronautics and Space Administration (NASA). Practically, Chl*a* is obtained after atmospheric correction by the OC4v6 algorithm (modifications of O'Reilly et al., 2000). The Chl*a* record is mapped on 5′-resolution cylindrical equidistant grids (9.26 km at the equator) for the period November 1997 to October 2007. The analysis is conducted on aggregations of 3×3 grid cells (corresponding to a resolution of 27-km) to increase the spatial coverage and reduce the noise but the main observed patterns are otherwise not affected (not shown). On a global scale, the uncertainties associated with this Chl*a* product have been assessed as a root-mean-square difference of 0.31 for log-transformed data (Gregg and Casey, 2004; this is likely lower for the reprocessed product used here), but it is acknowledged that higher discrepancies can be found at regional scales, particularly in coastal waters (see, e.g., Hyde et al., 2007; Mélin et al., 2007, and references therein). This problem is mitigated by focusing the analysis on open ocean waters, to the exclusion of coastal waters and regional seas. Some biases might still exist in specific regions but should not affect the large-scale analysis performed in this work that is focusing on relative temporal variations.

As ancillary data, a coincident series of sea surface temperature (SST) is obtained from the Physical Oceanography Distributed Active Archive Center (PODAAC, NASA) as the Pathfinder data set (version 5, Evans et al., 2009). The data are mapped on a 4-km equidistant grid. Only the grid points with the highest level of quality flags are considered in the analysis.

2.2. Climate indices

Climate indices are integrated descriptors of one or more facets of climate variations on various spatial scales that have proved helpful in interpreting time series of ecological variables (Stenseth et al., 2003; Martinez et al., 2009). Some are used here to provide background information with respect to the observed variability in Chl*a* (see Section 4). Table 1 provides the list of indices that are mentioned in the text, together with their sources and other appropriate information.

2.3. Statistical analysis

This sub-section provides a detailed description of the statistical approaches used in the study.

2.3.1. Data pre-processing

The statistical analysis is conducted at the level of each grid point, taking into account the spatial variations in the temporal coverage of the data record. Specifically, there are regions with persistent cloud cover and/or a high solar zenith angle, conditions leading to the absence of satellite coverage. In practice, if valid data values for a given month m (for example January) and grid point are present less than 50% of the years (over a potential maximum of 10), all values for m are removed, in effect creating for that grid point time series with an annual cycle of varying length, or period, $p\leq12$ (for the example, from February to December). Among these series, those with more than 25% of missing values are excluded.

The remaining missing data have been filled using the eigenvectors filtering method described in Ibanez and Conversi (2002) that is based on the use of orthogonal components reflecting the major temporal patterns of the original data. This iterative procedure consists in applying a series of principal component

[1] see http://oceancolor.gsfc.nasa.gov/REPROCESSING/R2009/

analyzes (PCA) computed on an auto-covariance matrix based on the original series, plus several replicates of it lagged progressively in time. The missing data are then estimated from the combination of the filtered series derived from the major principal axes and eigenvectors extracted from the PCA. This method has the advantage of preserving the temporal structure imbedded in the series.

2.3.2. Trend detection

The presence of monotonic upward or downward trends in the Chl*a* time series has been assessed using the non-parametric seasonal Kendall test. It is especially suitable for non-normally distributed data, data with missing values and outliers, or non-linearity, and it also accounts for seasonality in the time series (Gilbert, 1987). The null hypothesis H_0 assumes the randomness of the data set X and of X_m, the seasonal sub-samples of X (i.e., here the monthly sub-series, with $m=1,2,\ldots,p$).

The test is based on the computation of a suite of Mann–Kendall statistics (S_m) applied to each separated month m which are then combined to conclude on the presence of long-term monotonic changes in the original time series (Hirsch et al., 1982):

$$S_m = \sum_{i=1}^{nm-1} \sum_{j=i+1}^{nm} sgn(X_{jm}-X_{im}) \quad (1)$$

where nm is the number of valid data for the month m, and $sgn(X_{jm}-X_{im})=1$ if $X_{jm}-X_{im}>0$, 0 if $X_{jm}-X_{im}=0$, and -1 if $X_{jm}-X_{im}<0$.

The overall test result is equal to the sum of the monthly statistics: $S=\sum_{m=1}^{p} S_m$ and would follow, under the null hypothesis and for a large data set, a normal distribution of mean 0 and variance Var(S) (computed as in Hirsch et al., 1982).

The standardized value of S, denoted Z, is then computed as

$$Z=\begin{cases}(S-1)/\sqrt{Var(S)} & \text{if } S<0\\ 0 & \text{if } S=0\\ (S+1)/\sqrt{Var(S)} & \text{if } S>0\end{cases} \quad (2)$$

A positive value for Z indicates a monotonic upward trend while a negative value reveals a downward trend in the series. The null hypothesis H_0 is rejected at level α if $|Z|\geq Z_{1-\alpha/2}$ (two-tailed test).

The magnitude of the trend is evaluated by the non-parametric slope estimator adapted by Hirsch et al. (1982) from Sen (1968) which is robust against extreme values and seasonality in contrast to a classical linear slope estimator (Gilbert, 1987). The Sen's slope (β, expressed in % yr^{-1}) is the median of individual slopes, b_{mij}, found for each monthly sub-sample:

$$b_{mij}=\left[\frac{X_{mj}-X_{mi}}{j-i}\right] \quad (3)$$

for all pairs (X_{mj}, X_{mi}) with $m=1,2,\ldots,p$ and $1\leq i<j\leq nm$.

2.3.3. Time series decomposition

A record of values X(t) can be decomposed as (Shiskin et al., 1967):

$$X(t)=S(t)+T(t)+I(t) \quad (4)$$

where S, T and I represent, respectively, the seasonal signal, the trend (or trend-cycle), and an irregular (or residual) component.

The Census X-11 procedure (Shiskin et al., 1967) results from numerous modifications and improvements of the early decomposition "Method I" and then "Method II" developed in the 1950s and 1960s at the US Bureau of Census. This method is currently used as a standard tool in economics. The latest versions include various refinements mostly useful for diagnostic and modelling purposes (Findley et al., 1998), but the core of the procedure has remained very close to the initial X-11 algorithm. In this study, the decomposition of the data time series is performed using a simple version of the Census X-11 method that was recently adapted by Pezzulli et al. (2005) for application to time series of sea surface temperature (SST) at global scale, and that appears suitable for large scale computations.

The X-11 algorithm applied to any time series $X(t)$ of specific periodicity p can be decomposed into three successive steps (Pezzulli et al., 2005) that are now described for completeness:

- *Initial estimates*:
  - (a) A first estimate of the trend-cycle component is obtained from the annual-centered running average of the initial series $X(t)$. If p, the specific periodicity of the time series, is even, then $T(t)=MA_{2\times p}(X(t))$ with
  $$MA_{2\times p}(X(t))=[X(t-(p/2))+2X(t-(p/2)-1)+\cdots+2X(t)+\cdots+2X(t+(p/2)-1)+X(t+(p/2))]/2p \quad (5)$$
  If p is odd, a symmetric filter MA_p is used, with $MA_p(X(t))=(\sum_{\tau=t-(p/2)}^{t+(p/2)} X(\tau))/p$.
  - (b) A seasonal running mean ($SMA_{2\times 2}$) is then applied to the trend-adjusted series ($X(t)-T(t)$) to derive seasonal coefficients avoiding any confusion with inter-annual (trend) signal. The seasonal running mean for sub-series for the month m is
  $$SMA_{2\times 2}(X_{i,m})=\frac{(X_{i-1,m}-T_{i-1,m})+2(X_{i,m}-T_{i,m})+(X_{i+1,m}-T_{i+1,m})}{4} \quad (6)$$
  where $(X_{i,m}-T_{i,m})$ is the series sub-sample for each month $m=1,2,\ldots,p$ and the year $i=1,\ldots,n$.
  The resulting series is then normalized by subtracting its annual-centered running mean (see step (a)) leading to a seasonal series with approximately a null mean value for any of its sub-series of p consecutive terms.
- *Revised estimates*:
  - (c) An improved estimate of the trend component $T(t)$ is obtained by applying, similarly to the step (a), an annual filter to the seasonally adjusted series ($X(t)-S(t)$). However, in this case the simple annual-centered running average is replaced by a Henderson (1916) trend filter of weight $h=2p-1$. This filter operates a good smoothing action while preserving the local polynomial trends of orders 2 and 3.
- *Final estimates of the trend and irregular components*:
  - (d) The step (b) is repeated on the revised trend-adjusted series ($X(t)-T(t)$) to derive a refined final estimate of the seasonal component, $S(t)$.
  - (e) The final estimate of the trend component T(t) is obtained by repeating the step (c) on the revised seasonally adjusted series ($X(t)-S(t)$).
  - (f) The residual series that accounts for sub-annual variations is computed as $I(t)=X(t)-S(t)-T(t)$.

Importantly, the Census X-11 algorithm produces improved estimates of both seasonal and trend terms which are computed alternatively, allowing a proper separation of these two signals. An important feature of the Census X-11 procedure is that the seasonal term is determined locally in time, ensuring that the annual cycle of each year is not biased by uncorrelated events occurring at other times. Simultaneously, this allows inter-annual variations in the shape of the annual cycle contrarily to a climatological description of seasonality (i.e., a fixed annual cycle, Vantrepotte and Mélin, 2009, 2010). An implication is that

the trend-cycle term $T(t)$ does not contain any additional (and improper) variations related to inter-annual changes in seasonality. Consequently, the X-11 trend-cycle component is able to reproduce more properly long-term evolution in the mean level of the variable under study, and it has been shown to be particularly well adapted to model climate variations (Pezzulli et al., 2005).

The total variance σX^2 of the original time series X can now be written as

$$\sigma X(t)^2 = \sigma S(t)^2 + \sigma T(t)^2 + \sigma I(t)^2 + 2\, cov(S(t),T(t),I(t)) \quad (7)$$

where $\sigma S(t)^2$, $\sigma T(t)^2$ and $\sigma I(t)^2$ are the variance associated with the seasonal, trend and irregular components, respectively and $cov(S,T,I)$ includes the covariance terms between these three components. Considering that the covariance terms account for only a small percentage of the total variance (typically $<5\%$ in absolute value), the relative contribution ρ_z^2 of each component z (where $z = S$, T or I) to the total variance of the signal (expressed in %) can be approximated as $\rho_z^2 = 100\sigma z^2/\sigma X^2$.

This time series decomposition is performed on both Chl*a* and SST data records.

3. Results at global scale

3.1. Monotonic trend analysis

The focus of this sub-section is the identification of the open ocean regions presenting significant long-term monotonic changes in Chl*a* over the SeaWiFS period. The slope of the monotonic trend (expressed in % yr^{-1}) over 10 years of SeaWiFS data is shown in Fig. 1, with Fig. 1b displaying only the areas with a statistically significant trend ($p<0.01$). The absence of data coverage for the grid points at high latitudes is explained by the filtering conditions on the number of valid data records (see Section 2.3.1).

A strong negative Chl*a* trend is found in most of the subtropical gyre areas, namely the tropical North Atlantic, the southwestern part of the South Atlantic gyre (from -1% to $-3\%\ yr^{-1}$), the southeast Indian Ocean (-2% to $-3\%\ yr^{-1}$), a large part of the northern tropical Pacific as well as the south Pacific gyre (from -3% to $<-5\%\ yr^{-1}$). It is also seen in smaller areas like the eastern sector of the Southern Ocean, south of Africa (40–50°S, -1 to $-3\%\ yr^{-1}$). A strong decrease in the Chl*a* level is found for a large area of the Northeast Atlantic (40–55°N; 10–30°W), with a trend amplitude varying from $\approx -3\%$ to $<-5\%\ yr^{-1}$.

Areas with a statistically significant positive trend (Fig. 1) include the southern part of the Arabian Sea (+2% to +4% yr^{-1}), Pacific areas offshore North and South America (+1% to +3% yr^{-1}), and regions located south of Australia (+2% to +5% yr^{-1}). Additionally, the 10-year data set shows a significant increase in Chl*a* in a large region located in the northern part of the South Atlantic gyre (from +1 to +4% yr^{-1}, 15–30°N; 20°W–5°E) that contrasts with the decrease found southwest of this oceanic domain. The strongest upward Chl*a* trends among the open ocean regions are found southeast of Australia (i.e., Tasman Sea) with trend slopes being $\geq +5\%\ yr^{-1}$.

These results are generally comparable with past studies, among others, with those of Behrenfeld et al. (2006) over the

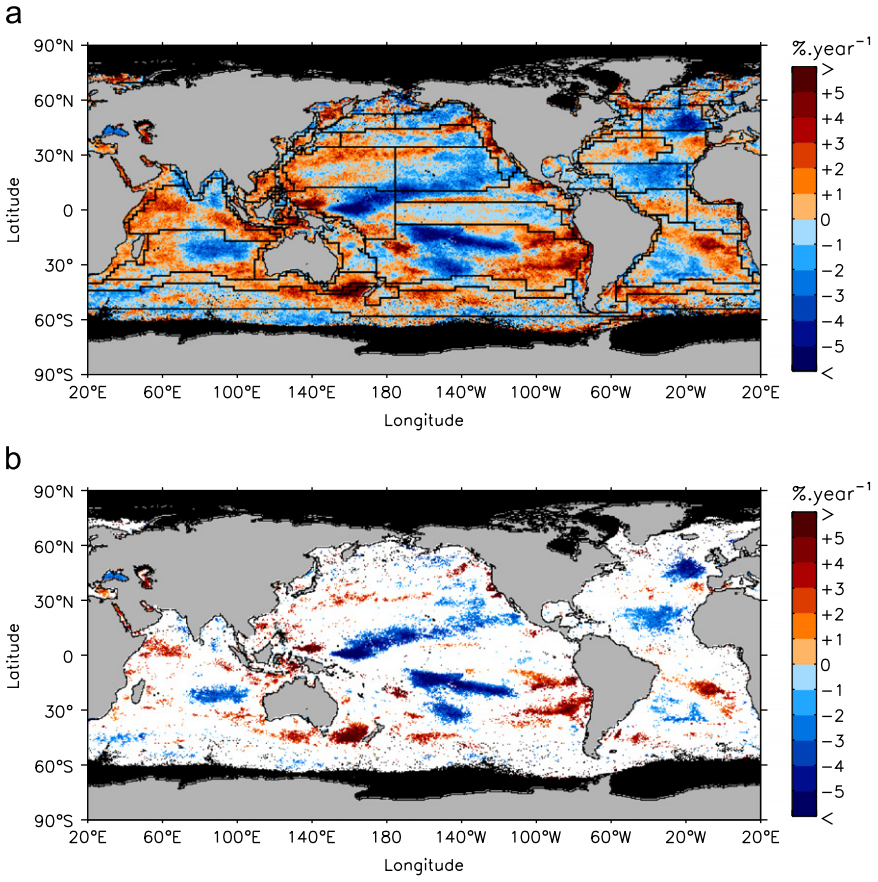

Fig. 1. Trend in phytoplankton Chl*a* over the 10-year SeaWiFS time period detected considering all the grid points (a) and displaying only the significant values detected from non-parametric seasonal Kendall statistics ($p<0.01$). The boundaries of the ecological and biogeochemical provinces by Longhurst (2007) are reported as black lines (a).

period 1997–2006 (with trends illustrated in terms of depth-integrated Chl*a* or primary production without distinguishing levels of statistical significance), and of Henson et al. (2010). They are also similar to the results obtained by Vantrepotte and Mélin (2009) with a simple linear regression on the deseasonalized series (from a previous version of the SeaWiFS record), even though the patterns with a statistically significant signal are fewer and smaller in the present case based on the Kendall statistics. It is interesting to note that some of the large areas of the ocean, identified as separate provinces (*sensu* Longhurst, 2007, Fig. 1a), may display two large-scale patterns of opposite trends (e.g., South Atlantic or South Pacific), emphasizing the need to study these patterns at an appropriate scale. Finally it is underlined that the monotonic trends detected over a decade currently cannot be attributed to global climate change (Henson et al., 2010), but could just be the signature of natural oscillations of frequency shorter or longer than 10 years. In fact it is the objective of the current study to document those temporal variations that are ultimately responsible for the presence of significant changes over the decade.

3.2. Census X-11 seasonal and trend terms

Fig. 2 shows the global distribution of the relative contribution of the variance associated with the Census X-11 seasonal and trend-cycle terms to the total variance of Chl*a*, respectively ρ_S^2 and ρ_T^2.

The seasonal cycle dominates the Chl*a* signal in the mid-latitude regions where ρ_S^2 can represent up to 95% of the total Chl*a* variance. Globally, the X-11 procedure, that allows variations in the annual cycle, captures a greater part of variance than classical time series decomposition approaches that assume a strictly periodical annual cycle (Vantrepotte and Mélin, 2009). From the X-11 output, the global average value for ρ_S^2, computed over all grid points, equals 64% ($\pm$15%), while it is only 36% ($\pm$19%) with the assumption of fixed seasonality (Vantrepotte and Mélin, 2009), demonstrating the benefit of the approach for studying phytoplankton phenology. Moreover, the spatial variations found in the increment of seasonal variance induced by the use of the X-11 procedure provide indications on the stability of the phytoplankton seasonal fluctuations. For instance, the maximum increment in variance induced by allowing a variable annual cycle is detected in the Equatorial Pacific ($\approx +40\%$ of variance) revealing the importance of inter-annual variations of the annual cycle in this region, while the increment is only 17% in the Mediterranean Sea characterized by a very regular phytoplankton seasonal cycle. More details are given on this topic by Vantrepotte and Mélin (2009).

Logically, the very high values for ρ_S^2 found in the sub-tropical bands are accompanied by relatively low contributions for the trend-cycle, with $\rho_T^2 < 15\%$ (Fig. 2(b)). Conversely, the trend-cycle term is a major contributor to the Chl*a* temporal variance in equatorial and tropical waters indicating a large inter-annual variability in these areas. The largest relative contribution of *T* to the total variance of the Chl*a* signal is seen in the tropical and equatorial Pacific, specifically in large areas of the North Pacific Equatorial Countercurrent province, the Western Pacific Warm Pool, and the northern part of the South Pacific Subtropical Gyre,

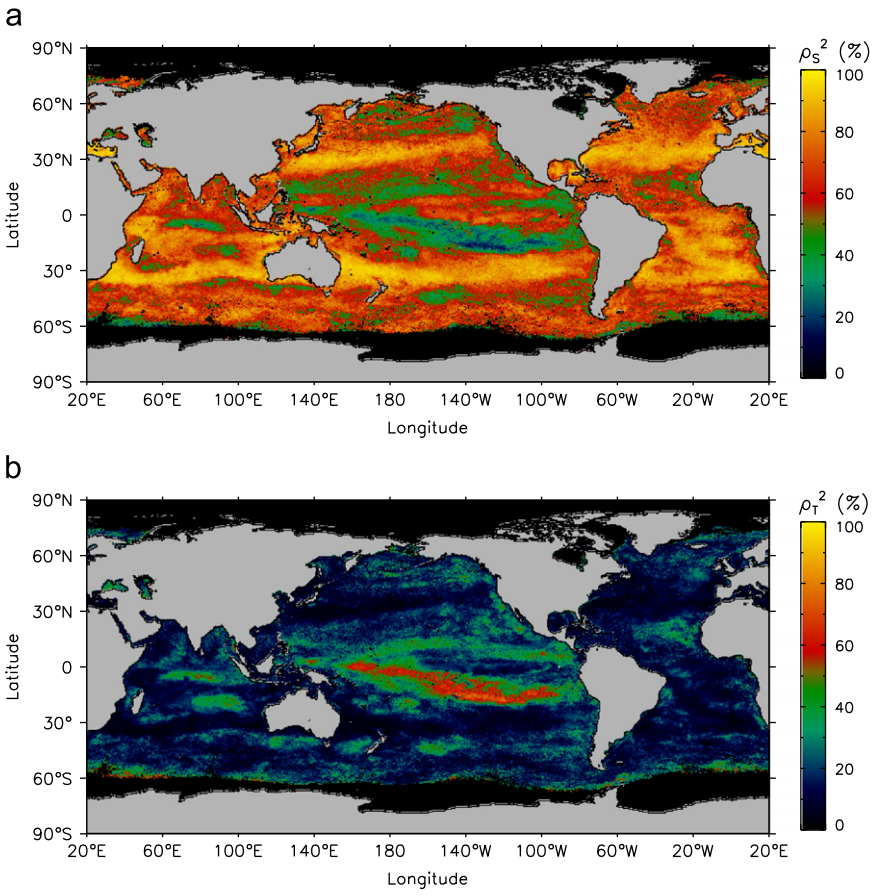

Fig. 2. Maps of the relative contribution to the total variance of the Chl*a* signal of (a) the seasonal component (ρ_S^2) and of (b) the trend component (ρ_T^2), derived from the X-11 temporal decomposition procedure (in %).

with ρ_T^2 values varying from 40% up to 75%. To a lesser extent, a relatively strong trend-cycle component is found in the equatorial Atlantic as well as in two large areas located in the Indian Ocean, in the equatorial band and the southern subtropical gyre (ρ_T^2 40–50%). Finally, patches of high ρ_T^2 are visible in some isolated areas, such as the convergence zone of the Southern Ocean or various coastal regions.

3.3. Patterns of interest and trend shape

In Sections 3.1 and 3.2, areas where Chl*a* levels have experienced major (monotonic and non-monotonic) long-term changes during the last decade have been identified with two distinct approaches. The agreement between the trend results delivered by the seasonal Kendall analysis and the X-11 procedure is however not systematic (compare Figs. 1 and 2). Some regions may show a strong X-11 trend component (i.e., high ρ_T^2) whereas no significant long-term monotonic change can be detected, and vice versa, depending on how these statistical models represent diverse inter-annual signals.

We propose to use the information delivered by these two methods to identify areas presenting relevant inter-annual patterns in phytoplankton biomass, and to derive more complete regional statistics needed to investigate the nature of the observed changes in Chl*a*. In practice, a distinction is done between time series showing:

1. a significant increasing monotonic trend associated with a strong (1a) or a weak (1b) X-11 trend-cycle component,
2. no significant monotonic change associated with a strong X-11 trend-cycle component,
3. a significant decreasing monotonic trend associated with a strong (3a) or a weak (3b) X-11 trend-cycle component.

This classification requires defining the strength of the trend-cycle T. The value of ρ_T^2 seems a relevant indicator for this classification but it is modulated by the contribution of the annual cycle to the total variance, ρ_S^2, itself very variable in space particularly with latitude (Fig. 2a). At mid to high latitudes, a significant inter-annual variation might still be associated with a low ρ_T^2, the Chl*a* signal being dominated by the annual cycle (Longhurst, 1995), whereas ρ_S^2 is generally lower at low latitudes. To account for these differences, the global ocean is partitioned into three biomes according to Longhurst (2007), i.e., polar biome, westerlies or mid-latitude biome, trade winds or low latitude biome (excluding the coastal biome from the analysis). For each biome, $\overline{\rho_T^2}$ and $\sigma(\rho_T^2)$ are calculated as the average and standard deviation of ρ_T^2, respectively. A grid point is classified as exhibiting a relatively strong trend-cycle if ρ_T^2 is larger than the threshold $\sigma(\rho_T^2)+\overline{\rho_T^2}$. Modifying this threshold within reasonable bounds does not affect the main results described below (not shown).

Fig. 3 shows the spatial distribution of the resulting classes with specific color codes (1a and b, 2, 3a and 3b). The boundaries of the major oceanic regions of interest (ROIs, individuated by a rectangle), selected to encompass the most relevant patterns and to derive average time series, are over-plotted on the figure: seven areas in the Pacific Ocean (P1 to P7), three in the Atlantic Ocean (A1 to A3) and in the Indian Ocean (I1 to I3), and five in the Southern Ocean (S1 to S5). Even though the choice of the ROIs is not exhaustive, it considers the main areas with a relevant signal in each oceanic basin and illustrates the variety of the trend patterns that can be identified from the X-11 outputs.

Considering the different classes existing within each ROI, regional statistics are computed for the total signal X and the X-11 seasonal and trend terms. Distinguishing the classes 1a and 1b, or 3a and 3b, does not provide additional information regarding the shape of the regional average time series (not shown). Therefore statistics are presented jointly for the classes 1a and 1b, and 3a and 3b. The spatial averages and standard deviations are computed for the grid points of a given class (or color) within a ROI, and thus represent statistics for a pattern of interest (POI) and not for the entire ROI. Patterns associated with classes are noted with the superscripts '+', '0' and '−' (positive, non-significant, and negative monotonic trends, respectively, as defined in Section 3.1).

The average regional series are computed from normalized individual series (associated with single grid points), with $X(t)$ and $T(t)$ normalized by their mean, and $S(t)$ and $I(t)$ normalized by their standard deviation. The analysis thus focuses on the shape of the temporal variations, independently of their actual amplitude. Potential outliers for each monthly statistics are removed by excluding data points lying further than three standard deviations from the regional mean. Moreover, monthly statistics associated with sparse data coverage are excluded: for a given month and area (i.e., each pattern for each ROI), the record is not considered

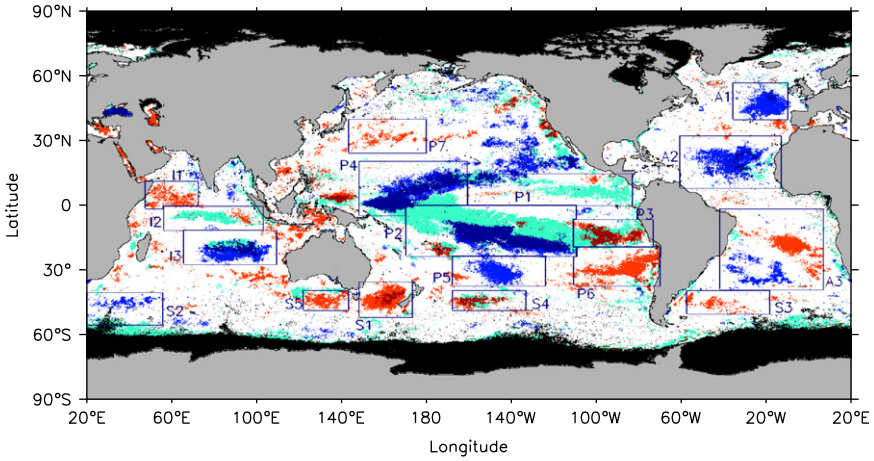

Fig. 3. Classification resulting of the comparison between results of the classical trend analysis and those of the Census X-11 derived trend term: (1) a significant increasing monotonic trend associated with a strong (a, dark red) and a weak (b, light red) X-11 trend-cycle component, (2) no significant monotonic change associated with a strong X-11 trend term (green), (3) a significant decreasing monotonic trend associated with a strong (a, dark blue) and a weak (light blue, b) X-11 trend-cycle component. Boundaries of the regions of interest considered for regional statistics for the X-11 terms are overlaid in blue line for the Pacific ocean (regions P1 to P7), the Atlantic Ocean (regions A1 to A3), the Indian Ocean (I1 to I3) and the Southern ocean (regions S1 to S5).

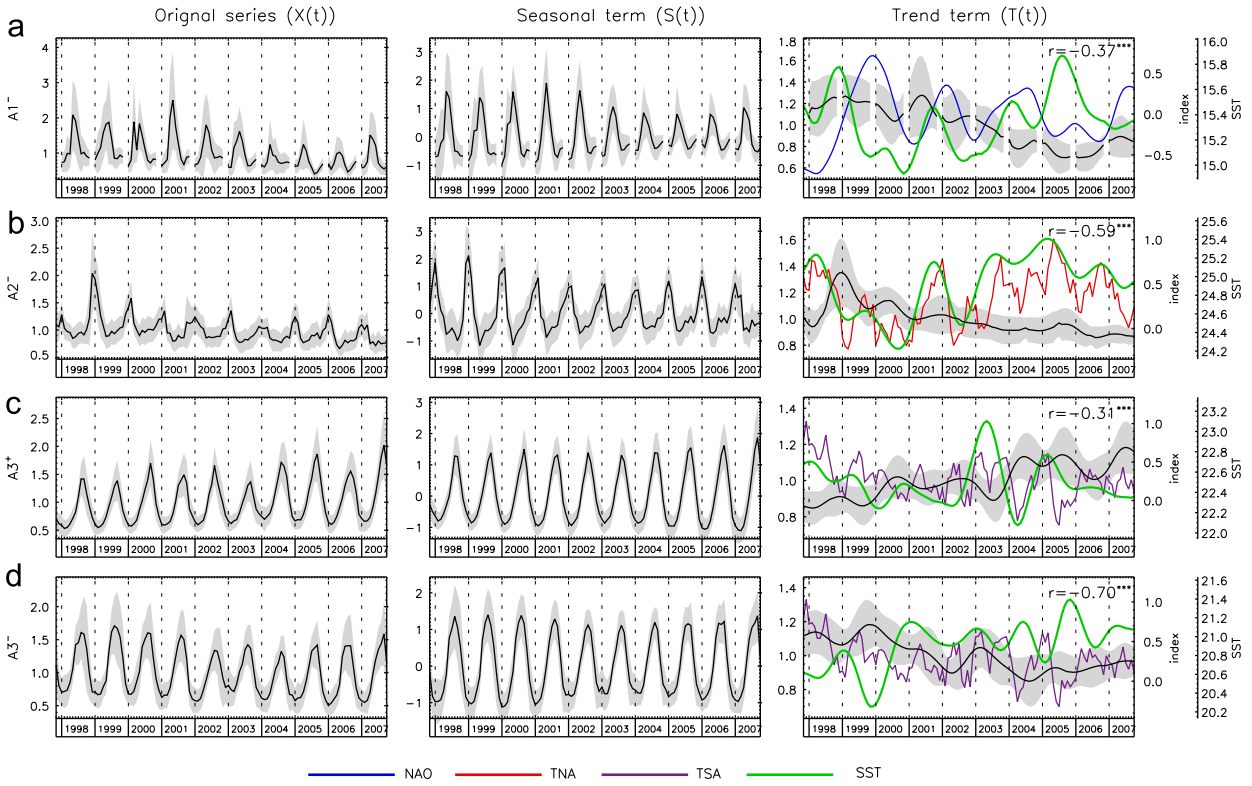

Fig. 4. X-11 terms regional statistics associated with the patterns of interest of the Atlantic Ocean: (a) A1$^-$, (b) A2$^-$, (c) A3$^+$, and (d) A3$^-$ (see definition of the regions in Fig. 3). From the left to the right, panels show the average normalized time series for $X(t)$, $S(t)$ and $T(t)$ (black line), respectively, with the envelope figuring the dispersion of the data around the regional average signal ($\bar{x} \pm \sigma$). Climate indices and average SST X-11 trend-term (see text) associated with each POI are over-plotted on the $T(t)$ time series (right-hand axis). The correlation coefficient between the regional average Chl*a* and SST X-11 trend signals is reported on the right-hand figure with the associated level of significance: '$*$' : $p < 0.05$," $**$" : $p < 0.01$," $***$" ,$p < 0.001$, otherwise: not significant.

if the valid data cover less than 60% of the total number of pixels composing the area. The average trend term $T(t)$ obtained for SST is also computed over each POI, and is then scaled by the overall average SST.

The average time series for the POIs selected in the Atlantic, Pacific, Indian and Southern oceans are presented in Figs. 4, 5, 6, and 7, respectively. In general, a relatively low dispersion (quantified as standard deviation and represented by gray envelopes) is found around the regional average signal. For instance for $T(t)$, mean coefficients of variation (ratio of standard deviation and average) vary from 11% to 17%, from 10% to 18%, from 11% to 15% and from 9% to 14% for the regions identified in the Pacific, Atlantic, Indian and Southern oceans, respectively, while maximum values do not exceed 32%. This underlines the relative homogeneity of the trend patterns within the selected areas, which is a remarkable result considering the very large extent of some of the considered ROIs (Fig. 3).

The classes introduced above are variously illustrated in Figs. 4–7. Some regions show a continuous change in their mean level of Chl*a* while the seasonal fluctuations remain stable in time. These areas are mainly associated with a X-11 trend-term of relatively low variance (classes 1b and 3b, Fig. 3). A second category includes areas presenting a strong trend-cycle term of the Chl*a* signal (i.e., high ρ_T^2) that is more like a shift or peak events. The latter case might be associated with an actual change in the average Chl*a* level over the period investigated, expressed by a statistically significant monotonic linear trend (classes 1a or 3a, Fig. 3). However, this is not systematic, with the cases of class 2, that are relevant inter-annual variations not picked up by a linear trend analysis. Finally, the observation of the averaged quasi-periodic X-11 seasonal term reveals that significant linear trends detected in some regions are associated with a change in the amplitude of the Chl*a* seasonal variations. These patterns are detailed for each oceanic basin in the next section.

4. Results at basin scale

In Figs. 4–7, left-hand, central and right-hand columns show, respectively, the total, seasonal and trend-term series. For the latter, the trend-terms T are shown for both Chl*a* and SST. When assessing the relationships between different series, Pearson's correlation is used with its associated level of significance. All correlation coefficients indicated are highly significant ($p < 0.001$), unless specified otherwise.

4.1. Atlantic ocean

As anticipated in Section 3.1, a large area of the Northeast Atlantic (approximately centered at 48°N–20°W, ROI A1$^-$, Fig. 4(a)) is characterized by a statistically significant monotonic trend ($\approx -3\%$ to $< -5\%\,\mathrm{yr}^{-1}$). The result of the X-11 temporal decomposition shows that it is associated with a decline of the trend-term T between 2001 and 2004 and contemporaneously with a clear decrease in the amplitude of the Chl*a* seasonal fluctuations: the amplitude of the annual cycle S averaged over 2003–2007 is 42% lower than the average over 1998–2002. The Northeast Atlantic appears prone to inter-annual (including decadal) biological variability. Particularly, the regime shift affecting this region (as well as the North Sea) in the mid-1980s has been well documented and included an abrupt increase in phytoplankton biomass (e.g., Reid et al., 1998; Raitsos et al.,

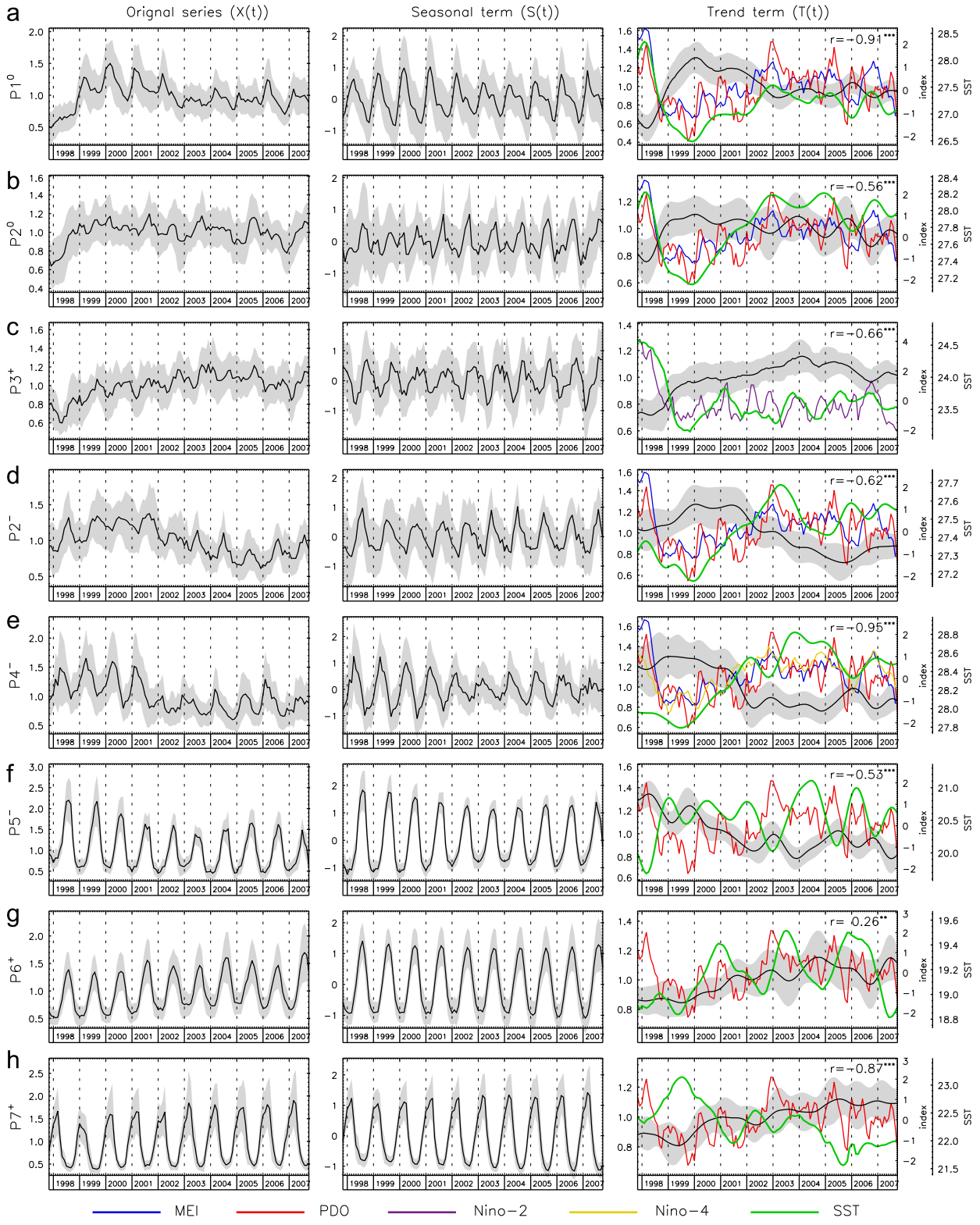

Fig. 5. As Fig. 4, with the X-11 terms regional statistics associated with the patterns of interest of the Pacific Ocean: (a) $P1^{o}$, (b) $P2^{o}$, (c) $P3^{+}$, (d) $P2^{-}$, (e) $P4^{-}$, (f) $P5^{-}$, (g) $P6^{+}$, and (h) $P7^{+}$.

2005) and changes in species composition (Leterme et al., 2006). Computed from Coastal Zone Color Scanner (CZCS, 1978–1986) and SeaWiFS data processed in a consistent manner (Antoine et al., 2005), the difference between the two Chl*a* records averaged over 1999–2002 (SeaWiFS) and 1979–1981 (CZCS) shows a large positive signal in a location strikingly similar to $A1^{-}$, suggesting a reversal of past variations. Ecosystem changes affecting the Northeast Atlantic have been diversely related to climate indices like NAO (Drinkwater et al., 2003); compared to the 1980s and the first half of the 1990s, the NAO index was in a more neutral state between 1997 and 2007, but no significant correlation between NAO (Table 1) and the trend-term *T* has been

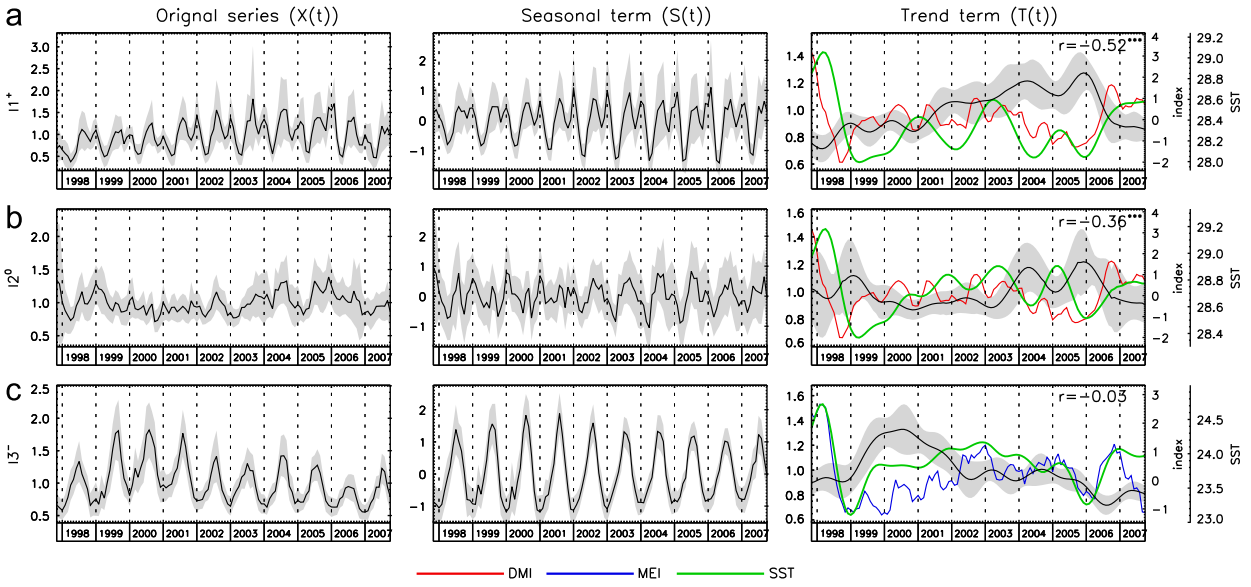

Fig. 6. As Fig. 4, with the X-11 terms regional statistics associated with the patterns of interest of the Indian Ocean: (a) $I1^{+}$, (b) $I2^{o}$, and (c) $I3^{-}$.

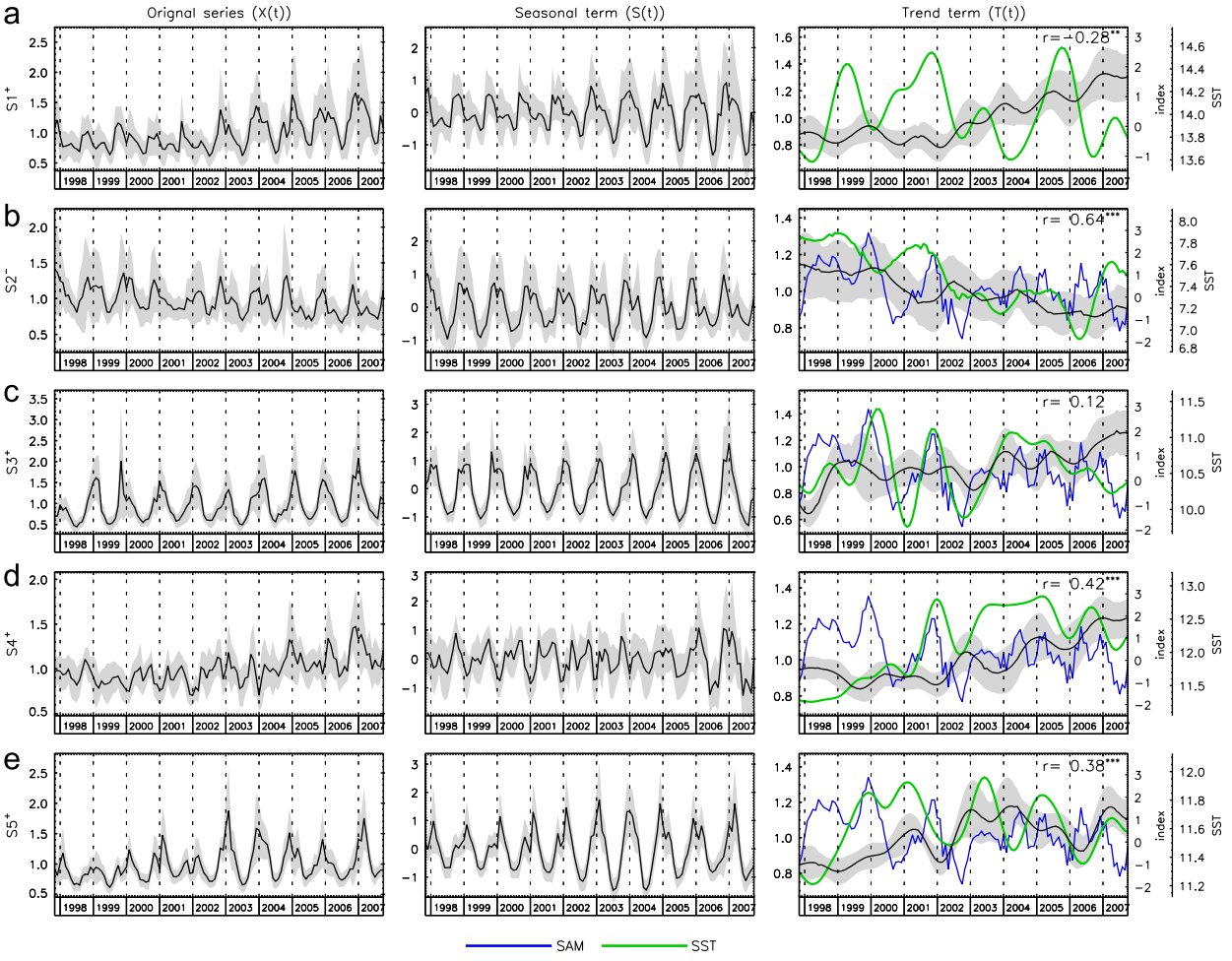

Fig. 7. As Fig. 4, with the X-11 terms regional statistics associated with the patterns of interest of the Southern Ocean: (a) $S1^{+}$, (b) $S2^{-}$, (c) $S3^{+}$, (d) $S4^{+}$, and (e) $S5^{+}$.

found over that period. It is worth adding here that the timing of the North Atlantic bloom seems more directly related to NAO than its magnitude (Henson et al., 2009a). The relation between the trend-terms T of Chl*a* and SST is not clear even though their correlation is significant ($r=-0.37$). A more in-depth analysis is needed to unravel the mechanisms behind the pattern $A1^{-}$.

The inter-annual variations in Chl*a* in the tropical North Atlantic show a reduced amplitude of the annual cycle after 2000 (−39% from the period 1998–2000 to 2001–2007) and a steady decrease of the trend-term *T* after a peak in the winter 1998–1999 (region A2, Figs. 3 and 4(b)). The marked increase in *T* in 1998 mimics a similar pattern in the Equatorial Pacific (see Section 4.2), suggesting the impact of teleconnections in tropical dynamics (Wang et al., 2009). The region has experienced a general increase in SST and upper-ocean stratification (Behrenfeld et al., 2006; Good et al., 2007), evoking the effects of a diminished supply of nutrients in the euphotic layer. The Tropical Northern Atlantic (TNA, Fig. 4(b)) index, that represents SST anomalies in the region 55°W–15°W, 5°N–25°N, as well as the SST trend-term *T* document this increase in temperature after a minimum in 1999–2000. The Chl*a* *T* signal of the POI $A2^-$ is found negatively correlated with both TNA ($r=-0.38$) and the SST *T* series ($r=-0.59$). The inter-annual changes in SST in the tropical Atlantic have been linked to an intermingled set of factors including anthropogenic influence (Santer et al., 2006), natural variability and the radiative impact of dust aerosols transported from Africa (Foltz and McPhaden, 2008; Wong et al., 2008; Evan et al., 2009). These aerosols make ocean color remote sensing fairly challenging in that region, suggesting some caution in the results.

The ROI A3 (Fig. 3) contains two patterns of opposite trends in the northeast (increasing, $A3^+$) and southwest (decreasing, $A3^-$) South Atlantic subtropical gyre (Figs. 4(c) and (d)). Conversely, the amplitude of the Chl*a* annual cycle *S* for the region has known only small variations. The general evolution of both trend-terms *T* is monotonic to the exceptions of some low-frequency oscillations and a reversal of *T* in the southwest sector over the period 2005–2007 (Fig. 4(c)). The two patterns $A3^+$ and $A3^-$ appear to form a dipole with a high correlation coefficient ($r=-0.77$) and are correlated to the Tropical Southern Atlantic (TSA, Figs. 4(c) and (d)) index ($r=-0.56$ and +0.43 for $A3^+$ and $A3^-$, respectively), that quantifies SST anomalies over the box 30°W–10°E, 20°S–0°, in the northern fringe of the ROI A3. For the POI $A3^-$, the coincident decrease of Chl*a* with an increasing SST ($r=-0.70$, Fig. 4(d)) is consistent with a scenario of increased stratification and lower nutrient availability (Behrenfeld et al., 2006). Similarly, in the northeastern part of the ROI A3, the SST and Chl*a* *T* terms are negatively correlated ($r=-0.31$) but there are large departures in this relation (Fig. 4(c)). In that part of A3, the link between stratification, SST and Chl*a* might be additionally modulated by remote forcing from the productive West African coastal area (Signorini et al., 1999).

The four patterns illustrated in the Atlantic Ocean are characterized by a significant monotonic change over the period that reinforces the covariations between the trend-terms *T*. The correlation between Chl*a* *T* for the four POIs has an amplitude $|r|$ varying between 0.57 and 0.79, and are all negatively correlated with the corresponding *T* term for SST, but this does not necessarily entail that the observed patterns result from a coherent basin-scale phenomenon.

4.2. Pacific Ocean

In the Pacific Ocean, the largest patterns of interest are located in the subtropics. Two patterns in the tropical Pacific display values of ρ_T^2 above the selected threshold without being associated with a significant monotonic trend (Figs. 2 and 3, patterns in green). They occupy the eastern part of the north Pacific countercurrent province (pattern $P1^0$) and a large area going obliquely from the eastern part of the Warm Pool across the Pacific equatorial divergence ($P2^0$). These two patterns are away from the Equator in the eastern Pacific since this area is associated with a low value of ρ_T^2 despite the large phytoplankton blooms that can be observed centered on the Equator after El Niño events (Ryan et al., 2006). The two trend-terms *T* are well correlated ($r=0.84$) and show a large increase in 1998 and 1999 (Figs. 5(a) and (b)). This feature reflects the influence on the phytoplankton community of the El Niño event of 1997–1998 and the transition to the subsequent La Niña period (Chavez et al., 1999; Behrenfeld et al., 2001). In the ROI P1, *T* then decreases from 2000 to 2002, whereas *T* for $P2^0$ shows other inter-annual oscillations associated with subsequent El Niños (McPhaden, 2004, 2008) with peaks at the end of 2003 and 2005 and in the boreal winter of 2007. The link between biology and the physical oscillations of the Pacific tropics is quantified by the correlation coefficients found between the Chl*a* *T* series analyzed for the POIs $P1^0$ and $P2^0$ and regional climate indices (Figs. 5(a) and (b)) like the Multivariate ENSO Index (MEI, $r=-0.72$ and -0.75, respectively), and the Pacific Decadal Oscillation (PDO, $r=-0.56$ and -0.41, respectively). The Chl*a* *T* series are also well correlated with the equivalent series for SST (*r* equal to -0.91 and -0.56 for $P1^0$ and $P2^0$, respectively).

The pattern detected in the ROI P3 extends the pattern $P2^0$ eastward to the Peruvian coast (Fig. 3). The trend-term *T* displays a minimum in 1998 and a sharp increase in 1999, as for $P1^0$ and $P2^0$, but differently it keeps increasing steadily to the end of 2003 to start a slight decrease thereafter (Fig. 5(c)). This evolution is translated into a statistically significant positive monotonic trend over the period. No significant correlation is found with the MEI and PDO indices; however, a significant negative correlation ($r=-0.40$) is found with the Niño 1+2 SST anomaly index that reflects eastern tropical Pacific ENSO conditions, off the coasts of Peru and Chile, as well as with the POI-averaged SST *T* term ($r=-0.66$), a covariation strongly influenced by the first 2 years of the record (Fig. 5(c)).

In the ROIs P2 and P4, two patterns with a large negative monotonic trends are found (Figs. 1 and 3), in the northern central part of the South Pacific subtropical gyre (pattern $P2^-$) and from the western Pacific Warm Pool going northeastward along the southern fringe of the subtropical gyre (in P4, actually prolonged across the entire basin). The two patterns of the trend-terms exhibit different temporal evolutions: in the case of $P2^-$, *T* first increases in 1998–1999, and decreases steadily from the end of 2001 to 2005 (Fig. 5(d)), whereas for $P4^-$, there is a sharp downward shift in 2001, followed by rather stable values, with the exception of a peak at the end of 2005 contemporaneous with post-El Niño conditions (Fig. 5(e)). Moreover in the case of $P4^-$, the amplitude of the Chl*a* annual cycle appears reduced after 2001 (a reduction of 50% from 1998–2001 to 2002–2007). The SST and Chl*a* trend-term series appear inversely related, with correlation coefficients of -0.62 and -0.95 for $P2^-$ and $P4^-$, respectively. Moreover, the Chl*a* *T* series are significantly correlated with variations of the PDO index ($r=-0.39$ and -0.43, for the northern and southern Pacific, $P4^-$ and $P2^-$, respectively). This basin-scale oscillation that exerts an influence on marine ecosystems in a large part of the Pacific (Chavez et al., 2003), presented mostly negative values (cool phase) in 1998–2002 and positive values (warm phase) until 2005. The two subtropical patterns are also correlated with the MEI, albeit to a lesser extent ($r=-0.37$ and -0.32, respectively). Conversely, the $P4^-$ pattern appears well correlated with the Niño4 SST anomaly index ($r=-0.79$) describing the western tropical Pacific El Niño conditions (Fig. 5(e)).

Three patterns are selected at higher latitudes in the Pacific Ocean, one in the northwestern basin (POI P7), associated with a positive monotonic trend, and two contrasting patterns in the mid-latitude South Pacific, in the western central subtropical gyre (P5) and in the eastern part of the gyre abutting on the Chilean

upwelling (P6), associated with negative and positive trends, respectively (Figs. 1 and 3). The Chl*a* annual cycles, much more pronounced than for the tropical regions discussed previously, appear stable over the period, even though that of P7 show a slight increase in amplitude. Chl*a* trend-terms *T* are fairly monotonic with some oscillations (Figs. 5(f)–(h)). They are not significantly correlated with the MEI, and only the patterns $P6^+$ and $P7^+$ show a weak correlation with the PDO ($r=+0.32$ and $+0.33$, respectively). A common element found for these three patterns, as for the other Pacific POIs, is a negative correlation with the local trend-term of SST even though to a varying extent. The correlation for $P5^-$ ($r=-0.53$) seems to originate from a suite of inverse oscillations, whereas the result for $P7^+$ ($r=-0.87$) is influenced by higher SST *T* values in 1998–2000 and lower values in 2005–2007.

4.3. Indian Ocean

The Indian Ocean contains the three categories of patterns discussed in Section 3.3. The regional average statistics for the southwestern Arabian sea (pattern $I1^+$, Fig. 3) reveals that the detected significant increase in Chl*a* occurs mostly from 1998 to 2003 (Fig. 6(a)), whereas the Chl*a* trend-term experiences a sharp drop in 2006. In parallel, the intensity of the phytoplankton annual cycle, which shows typical bi-annual maxima, appears to increase significantly over the period investigated (by 60% from the period 1998–2000 to 2001–2007). Goes et al. (2005) related a significant increase in Chl*a* in the western Arabian Sea over the period 1998–2004 with stronger summer monsoon winds reinforced by the land–sea thermal gradient. The present results show that the trend in Chl*a* has been at least partly reversed in 2006–2007. Moreover, it did not affect the eastern Arabian Sea, as underlined also by Prakash and Ramesh (2007). A significant correlation ($r=-0.38$) is found with the Indian Ocean Dipole Mode Index (DMI, representing the SST east–west gradient, Fig. 6(a)). An inverse correlation is found with the ROI SST trend-term ($r=-0.52$) that shows a large drop in 1998, and individual inverse oscillations, particularly in the last 3 years of the period.

A pattern of high ρ_T^2 is detected in a large area of the central Indian Ocean (pattern $I2^0$, Fig. 3), whereas no significant linear trend in Chl*a* is detected over the period investigated. Rather the trend-term *T* shows isolated pairs of Chl*a* peaks (Fig. 6(b)). At the beginning of the series, *T* decreases and increases again to reach a maximum in January 1999, an oscillation related to the strong ENSO episode (Murtugudde et al., 1999). Two other peaks are observed in 2004 and 2005, a period with ENSO in a mostly warm phase (McPhaden, 2008) and a mostly negative state of the DMI. Coincident inverse peaks are seen for the SST trend-term, contributing to strengthen the overall relation between SST and Chl*a* *T* series over the period ($r=-0.36$). The Chl*a* trend-term *T* then decreases in 2006 and stays low in 2007, a period of positive DMI (Vinayachandran et al., 2007; Behera et al., 2008). This is translated into a significant negative correlation between *T* and the DMI ($r=-0.46$). On the other hand, there is no significant correlation with the ENSO MEI.

The region I3 (Fig. 3) encompasses a pattern in the southern subtropical gyre of the Indian Ocean with a significant monotonic trend of decreasing Chl*a* ($I3^-$, Fig. 1). The trend-term *T* reveals that the negative overall trend is due to a steady decrease in Chl*a* starting in 2000 (particularly marked from mid-2000 to mid-2002), whereas *T* shows a sharp increase in 1999 (Fig. 6(c)). Much of the Indian Ocean has experienced an increase in SST in the decades 1960–1990s (Alory et al., 2007), so that, as for other subtropical gyres, the observed changes in Chl*a* seem consistent with a scenario of increased stratification and decreased nutrient inputs (Behrenfeld et al., 2006). On the other hand, the Chl*a* trend-term decrease from 2000 to the end of 2005 merely brought its value back to that observed at the beginning of the series, and the Chl*a* and SST *T* terms are not correlated. Interestingly, the trend pattern *T* observed for this POI is very similar to its counterpart found in the southern subtropical Pacific (pattern $P2^-$, Fig. 5(e), $r=+0.81$) that is situated at a similar latitude. Differently than for the equatorial Indian Ocean (pattern $I2^0$), no significant correlation is found with the DMI, whereas the correlation with the MEI is $r=-0.38$.

4.4. Southern Ocean

A strong signal in terms of monotonic trend and ρ_T^2 (Figs. 1 and 2) is found in the Tasman Sea (pattern $S1^+$, Fig. 3). Examining the X-11 decomposition outputs, it appears that the overall increase in Chl*a* is prompted by a large steady increase of the trend-term *T* starting in 2002 after 4 years of stability (Fig. 7(a)). These variations are weakly correlated with the corresponding SST trend-term, even though the SST *T* is on average lower after 2002. Moreover, the Chl*a* annual cycle has an increasingly large amplitude after 2000 (an increment of 59% if considering averages over 1998–2002 and 2003–2007), and the nature of the annual cycle appears changed in the second half of the period considered. In the period 1997–2002, the annual cycle shows a primary austral spring bloom, followed by a secondary fall bloom (Murphy, 2001; Tilburg et al., 2002), whereas subsequent years display a broader single maximum. The Tasman Sea has experienced a trend in physical variables (e.g., increasing temperature and sea surface height) over the approximate period 1995–2002 (Sutton et al., 2005; Qiu and Chen, 2006) that is part of a general pattern of the South Pacific subtropical gyre (Roemmich et al., 2007). This has had an impact on the Tasman Sea marine ecosystem and fisheries (with a decline in the hoki stocks, Bradford-Grieve et al., 2004). This trend in physical variables has started reversing after 2002. The results presented here in terms of Chl*a* increase after 2002 might indicate a return to previous ecosystem conditions.

Four fairly small POIs are detected in the Southern Ocean at latitudes between 40°S and 55°S. In the western Indian Ocean sector of the Southern Ocean, a pattern of decreasing Chl*a* is detected southeast of Africa (pattern $S2^-$, Fig. 3), associated with a steady decrease of the trend-term *T* after 1999 (Fig. 7(b)). Conversely three patterns are related to an average Chl*a* increase, in the Atlantic sector offshore Patagonia, in the Pacific sector and south of Australia (S3, S4 and S5, respectively), that show diverse variations of *T*, with increases in 1998, 2003 and 2006 for S3 (Fig. 7(c)), an increase after 2002 for S4 (coincident with that displayed by S1) (Fig. 7(d)), and an average increase between 1999 and 2004 for S5 (Fig. 7(e)). These four Chl*a* *T* patterns tend to be positively correlated with the SST trend-term counterpart (*r* between +0.12 and +0.64), and are variously correlated with the Southern Annular Mode index (SAM, Figs. 7(b)–((e)) which is a dominant mode of atmospheric variability in the Southern Hemisphere (Marshall, 2003), with *r* equal to +0.32 ($p<0.001$), −0.19 ($p<0.05$), −0.31 ($p<0.001$) and −0.46 ($p<0.001$) for S2 to S5. They are also inter-related, with the correlation between S3, S4 and S5 varying between +0.45 and +0.55, and S2 anti-correlated with these three POIs (*r* from −0.63 to −0.70). Finally it is relevant to note that the region S2 might be affected by significant changes in terms of wind and ocean circulation (Cai, 2006; Biastoch et al., 2009), that might impact the light and/or nutrient supply of the phytoplankton population in the area.

5. Conclusions

The first achievement of this study is the selection of patterns showing a significant inter-annual variability across the global

ocean using the 10-year SeaWiFS-derived Chl*a* data series. The patterns of variations have been identified after decomposition of the Chl*a* signal into seasonal and trend components by the Census X-11 technique. This approach has proved to be a valuable tool to analyze the Chl*a* satellite-derived record in terms of variations in the annual cycle (*S*) and long-term evolutions (*T*). The selection of patterns of interest (POI) is based on the relative contribution of the trend-term to the total variance. Even though the test employed for selection could be refined, the set of selected POIs serves its purpose well and provides a framework to characterize the inter-annual changes affecting the Chl*a* record. The POIs analyzed are distributed in all major oceans except at high latitudes because of the restrictions associated with data availability. The identified POIs have been classified into three categories: some are associated with a significant monotonic trend, increasing or decreasing, whereas some others, mostly located in the tropical band, are not. These latter patterns would be ignored if considering only areas displaying a statistically significant monotonic change. An important result is that the series inside each POI show coherent variations.

The work has then proceeded with a comprehensive and detailed description of the inter-annual variations associated with each selected pattern. In most cases, a slope of linear regression appears as a very incomplete descriptor of change, and in fact, the most striking result of the present study is the diversity of trend patterns illustrated, even at the scale of sub-basins (Figs. 4–7). Some trend-terms are fairly monotonic over most (both A3 POIs in the South Atlantic, $P7^+$ in the Pacific, or $S2^-$ in the Southern Ocean) or only part ($A1^-$ in the Northeast Atlantic, or $S1^+$ in the Tasman Sea) of the period, whereas others display shifts or a set of multi-annual oscillations. Furthermore some time series show clear variations in the annual cycle ($A1^-$ and $A2^-$ in the North Atlantic, $P4^-$ in the Pacific, $I1^+$ in the Arabian Sea, $S1^+$ in the Tasman Sea).

Biogeochemical models experience difficulty in reproducing inter-annual trends and shifts in marine Chl*a* or primary production (e.g., Schneider et al., 2008; Henson et al., 2009b). The set of globally distributed patterns of inter-annual variability illustrated here (Figs. 4–7) appears as a template on which to test present and future models on their ability to faithfully represent phytoplankton large-scale multi-annual variations. Another related challenge is to identify the drivers behind these changes. Chl*a* variations may be the translation of changes in phytoplankton biomass, the Chl*a*-to-carbon ratio in algal cells or population floristic shifts (Behrenfeld et al., 2008; Boyd and Doney, 2002). These in turn result from a complex set of pressures (physical, chemical or biological top-down controls) that act on the entire marine ecosystem at various time scales. Correlation analyzes conducted here confirm that Chl*a* inter-annual signals can often be linked to climate indices (e.g., Bidigare et al., 2009; Martinez et al., 2009; Boyce et al., 2010) but more work is certainly needed to go beyond these representations. Linear trends of decreasing SeaWiFS-derived Chl*a* have been identified in subtropical gyres (e.g., Polovina et al., 2008), and discussed in the context of a scenario of warmer SST and increased stratification, whereas at higher latitudes the same scenario, with higher temperatures in cold waters and alleviated light limitation, might lead to an increase in Chl*a* (Behrenfeld et al., 2006; Doney, 2006). This scenario has received additional support by considering much longer, decade-long, time series derived from in situ data (Boyce et al., 2010). The correlation analysis applied to the Chl*a* and SST trend-terms and presented at the scale of each POI also tends to support this scenario, particularly for most subtropical regions. For higher latitudes, the results are contrasted, with a positive correlation coefficient significant only for S2, S4 and S5. As noted several times in the text, some high correlation coefficients are strengthened more by coincident pairs of individual oscillations than by the existence of overall simultaneous monotonic signals. Ultimately, the diversity of temporal patterns shown here (for Chl*a* and for its relation with SST) and the rather short time period considered (10 years) caution that more work is needed to validate the proposed scenario at the scale of separate regions, particularly in the context of climate change, and to unravel how other factors perturb it. Continuing this effort relies on the extension of the satellite temporal coverage and the creation of a multi-mission consistent climate-quality data record.

Acknowledgments

The authors would like to thank the Ocean Biology Processing Group (NASA) for the distribution of the SeaWiFS data and the PODAAC (Jet Propulsion Laboratory, NASA) for the availability of the Pathfinder SST data set. Pr F. Ibanez is acknowledged for his help and comments on the eigenvector filtering method.

References

Alory, G., Wijffels, S., Meyers, G., 2007. Observed temperature trends in the Indian Ocean over 1960–1999 and associated mechanisms. Geophysical Research Letters 34, L02606. doi:10.1029/2006GL028044.

Antoine, D., Morel, A., Gordon, H.R., Banzon, V.F., Evans, R.H., 2005. Bridging ocean color observations of the 1980s and 2000s in search of long-term trends. Journal of Geophysical Research 110, C06009. doi:10.1029/2004JC002620.

Beaugrand, G., Reid, P.C., 2003. Long-term changes in phytoplankton, zooplankton and salmon related to climate. Global Change Biology 9, 801–817.

Behera, S.K., Luo, J.-J., Yamagata, T., 2008. Unusual IOD event of 2007. Geophysical Research Letters 35, L14S11. doi:10.1029/2008GL034122.

Behrenfeld, M.J., Randerson, J.T., McClain, C.R., Feldman, G.C., Los, S.O., Tucker, C.J., Falkowski, P.G., Field, C.B., Frouin, R., Esaias, W.E., Kolber, D.D., Pollack, N.H., 2001. Biospheric primary production during an ENSO transition. Science 291, 2594–2597.

Behrenfeld, M.J., O'Malley, R.T., Siegel, D.A., McClain, C.R., Sarmiento, J.L., Feldman, G.C., Milligan, A.J., Falkowski, P.G., Letelier, R.M., Boss, E.S., 2006. Climate-driven trends in contemporary ocean productivity. Nature 444, 752–755.

Behrenfeld, M.J., Halsey, K.H., Milligan, A.J., 2008. Evolved physiological responses of phytoplankton to their integrated growth environment. Philosophical Transactions of the Royal Society B 363, 2687–2703.

Biastoch, A., Böning, C.W., Schwarzkopf, F.U., Lutjeharms, J.R.E., 2009. Increase in Agulhas leakage due to poleward shift of Southern Hemisphere westerlies. Nature 462, 495–498.

Bidigare, R.R., Chai, F., Landry, M.R., Lukas, R., Hannides, C.C.S., Christensen, S.J., Karl, K.M., Shi, L., Chao, Y., 2009. Subtropical ocean ecosystem structure changes forced by North Pacific climate variations. Journal of Plankton Research 31, 1131–1139.

Bopp, L., Aumont, O., Cadule, P., Alvain, S., Gehlen, M., 2005. Response of diatoms distribution to global warming and potential implications: a global model study. Geophysical Research Letters 32, L19606. doi:10.1029/2005GL023653.

Boyce, D.G., Lewis, M.R., Worm, B., 2010. Global phytoplankton decline over the past century. Nature 466, 591–596.

Boyd, P.W., Doney, S.C., 2002. Modelling regional responses by marine pelagic ecosystems to global climate change. Geophysical Research Letters 29. doi:10.1029/2001GL014130.

Bradford-Grieve, J., Livingston, M., Sutton, P., Hadfield, M., 2004. Ocean variability and hoki decline. Water and Atmosphere, NIWA Science 12, 20–21.

Cai, W., 2006. Antarctic ozone depletion causes an intensification of the Southern Ocean super-gyre circulation. Geophysical Research Letters 33, L03712. doi:10.1029/2005GL024911.

Chavez, F.P., Strutton, P.G., Friedrich, G.E., Feely, R.A., Feldman, G.C., Foley, D.G., McPhaden, M.J., 1999. Biological and chemical response of the Equatorial Pacific Ocean to the 1997–98 El Niño. Science 286, 2126–2131.

Chavez, F.P., Ryan, J., Lluch-Cota, S.E., Ñiquen, M.C., 2003. From anchovies to sardines and back: multidecadal change in the Pacific Ocean. Science 299, 217–221.

Doney, S.C., 2006. Plankton in a warmer world. Nature 444, 695–696.

Drinkwater, K.F., Belgrano, A., Borja, A., Convsersi, A., Edwards, M., Greene, C.H., Ottersen, G., Pershing, A.J., Walker, H., 2003. The response of marine ecosystems to climate variability associated with the North Atlantic Oscillation. In: Hurrell, J.W., Kushnir, Y., Ottersen, G., Visbeck, M. (Eds.), The North Atlantic Oscillation: Climate Significance and Environmental Impact. Geophysical Monograph Series of the American Geophysical Union, pp. 211–234.

Enfield, D.B., Mestas-Nuñez, A.M., Mayer, D.A., Cid-Serrano, L., 1999. How ubiquitous is the dipole relationship in tropical Atlantic sea surface temperatures? Journal of Geophysical Research 104, 7841–7848.

Evan, A.T., Vimont, D.J., Heidinger, A.K., Kossin, J.P., Bennartz, R., 2009. The role of aerosols in the evolution of tropical North Atlantic ocean temperature anomalies. Science 324, 778–781.
Evans, B., Vazquez, J., Casey, K.S., 2009. 4-km Pathfinder Version 5 user guide 〈http://www.nodc.noaa.gov/sog/pathfinder4km/PFV50_UserGuide.pdf〉.
Findley, D.F., Monsell, B.C., Bell, W.R., Otto, M.C., Bor-Chung, C., 1998. New capabilities and methods of the X-12-ARIMA seasonal-adjustment program. Journal of Business and Economic Statistics 16, 122–177.
Foltz, G.R., McPhaden, M.J., 2008. Trends in Saharan dust and tropical Atlantic climate during 1980–2006. Geophysical Research Letters 35, L20706. doi:10.1029/2008GL035042.
Gilbert, R.O., 1987. Statistical Methods for Environmental Pollution Monitoring. John Wiley and Sons, Inc, New York.
Goes, J.I., Thoppil, P.G., Gomes, H.G., Fasullo, J.T., 2005. Warming of the Eurasian land mass is making the Arabian Sea more productive. Science 308, 545–547.
Good, S.A., Corlett, G.K., Remedios, J.J., Noyes, E.J., Llewellyn-Jones, D.T., 2007. The global trend in sea surface temperature from 20 years of Advanced Very High Resolution Radiometer data. Journal of Climate 20, 1255–1264.
Gregg, W.W., Casey, N.W., 2004. Global and regional evaluation of the SeaWiFS chlorophyll data set. Remote Sensing of Environment 93, 463–479.
Gregg, W.W., Casey, N.W., McClain, C.R., 2005. Recent trends in global ocean chlorophyll. Geophysical Research Letters 32, L03606. doi:10.1029/2004GL021808.
Henderson, R., 1916. Note on graduation by adjusted average. Transactions on American Society Actuaries 17, 43–48.
Henson, S.A., Dunne, J.P., Sarmiento, J.L., 2009a. Decadal variability in North Atlantic phytoplankton blooms. Journal of Geophysical Research 114, C04013. doi:10.1029/2008JC005139.
Henson, S.A., Raitsos, D., Dunne, J.P., McQuatters-Gollop, A., 2009b. Decadal variability in biogeochemical models: comparison with a 50-year ocean colour dataset. Geophysical Research Letters 36, L21601. doi:10.1029/2009GL040874.
Henson, S.A., Sarmiento, J.L., Dunne, J.P., Bopp, L., Lima, I., Doney, S.C., John, J., Beaulieu, C., 2010. Detection of anthropogenic climate change in satellite records of ocean chlorophyll and productivity. Biogeosciences 7, 621–640.
Hirsch, R.M., Slack, J.R., Smith, R.A., 1982. Techniques of trend analysis for monthly water quality data. Water Resources Research 18, 107–121.
Hsieh, C.-H., Glaser, S.M., Lucas, A.J., Sugihara, G., 2005. Distinguishing random environmental fluctuations from ecological catastrophes for the North Pacific Ocean. Nature 435, 336–340.
Hurrell, J.W., 1995. Decadal trends in the North Atlantic Oscillation: regional temperatures and precipitation. Science 269, 676–679.
Hyde, K.J.W., O'Reilly, J.E., Oviatt, C.A., 2007. Validation of SeaWiFS chlorophyll *a* in Massachusetts Bay. Continental Shelf Research 27, 1677–1691.
Ibanez, F., Conversi, A., 2002. Prediction of missing values and detection of 'exceptional events' in a chronological planktonic series: a single algorithm. Ecological Modelling 154, 9–23.
Irwin, A.J., Oliver, M.J., 2009. Are ocean deserts getting larger? Geophysical Research Letters 36, L18609. doi:10.1029/2009GL039883.
Karl, D.M., Bidigare, R.R., Letelier, R.M., 2001. Long-term changes in phytoplankton community structure and productivity in the North Pacific Subtropical Gyre: the domain shift hypothesis. Deep-Sea Research, II 48, 1449–1470.
Kirby, R.R., Beaugrand, G., 2009. Trophic amplification of climate warming. Proceedings of the Royal Society, B 276, 4095–4103.
Leterme, S., Seuront, L., Edwards, M., 2006. Differential contribution of diatoms and dinoflagellates to phytoplankton biomass in the NE Atlantic Ocean and the North Sea. Marine Ecology Progress Series 312, 57–64.
Longhurst, A.R., 1995. Seasonal cycles of pelagic production and consumption. Progress in Oceanography 36, 77–167.
Longhurst, A.R., 2007. Ecological Geography of the Sea, second ed. Academic Press, San Diego 542 pp.
Mann, K.H., Lazier, J.R.N., 1996. Dynamics of Marine Ecosystems, second ed. Blackwell Science 394 pp.
Mantua, N.J., Hare, S.R., Zhang, Y., Wallace, J.M., Francis, R.C., 1997. A Pacific interdecadal climate oscillation with impacts on salmon production. Bulletin of the American Meteorological Society 78, 1069–1079.
Marshall, G.J., 2003. Trends in the Southern Annular Mode from observations and reanalyses. Journal of Climate 16, 4134–4143.
Martinez, E., Antoine, D., D'Ortenzio, F., Gentili, B., 2009. Climate-driven basin-scale decadal oscillations of oceanic phytoplankton. Science 326, 1253–1256.
McClain, C.R., Feldman, G.C., Hooker, S.B., 2004a. An overview of the SeaWiFS project and strategies for producing a climate research quality global ocean bio-optical time series. Deep-Sea Research, II 51, 5–42.
McClain, C.R., Signorini, S.R., Christian, J.R., 2004b. Subtropical gyre variability observed by ocean-color satellites. Deep-Sea Research, II 51, 281–301.
McPhaden, M.J., 2004. Evolution of the 2002/03 El Niño. Bulletin American Meteorological Society 85, 677–695.
McPhaden, M.J., 2008. Evolution of the 2006-2007 El Niño: the role of intraseasonal to interannual time scale dynamics. Advances in Geosciences 14, 219–230.
Mélin, F., Zibordi, G., Berthon, J.-F., 2007. Assessment of satellite ocean color products at a coastal site. Remote Sensing of Environment 110, 192–215.
Murphy, R.J., 2001. Phytoplankton distributions around New Zealand derived from SeaWiFS remotely-sensed ocean color data. New Zealand Journal of Marine and Fresh Waters Research 35, 343–362.
Murtugudde, R.G., Signorini, S.R., Christian, J.R., Busalacchi, A.J., McClain, C.R., Picaut, J., 1999. Ocean color variability of the tropical Indo-Pacific basin observed by SeaWiFS during 1997–1998. Journal of Geophysical Research 104, 18351–18366.
O'Reilly, J.E., Maritorena, S., Siegel, D.A., O'Brien, M.C., Toole, D.A., Mitchell, B.G., Kahru, M., Chavez, F.P., Strutton, P., Cota, G.F., Hooker, S.B., McClain, C.R., Carder, K.L., Mueller-Karger, F., Harding, L., Magnusson, A., Phinney, D., Moore, G.F., Aiken, J., Arrigo, K.R., Letelier, R., Culver, M., 2000. Ocean color chlorophyll *a* algorithms for SeaWiFS, OC2, and OC4: Version 4. In: S.B. Hooker and E.R. Firestone (Eds.), NASA-GSFC, NASA Technical Memorandum 2000-206892, vol. 20, Greenbelt, Maryland, 2000, pp. 9–23.
Pezzulli, S., Stephenson, D.B., Hannach, A., 2005. The variability of seasonality. Journal of Climate 53, 71–88.
Polovina, J.J., Howell, E.A., Abecassis, M., 2008. Ocean's least productive waters are expanding. Geophysical Research Letters 35, L03618. doi:10.1029/2007GL031745.
Prakash, S., Ramesh, R., 2007. Is the Arabian Sea getting more productive? Current Science 92 (5), 667–671.
Qiu, B., Chen, S., 2006. Decadal variability in the large-scale sea surface height field of the South Pacific Ocean: observations and causes. Journal of Physical Oceanography 36, 1751–1762.
Raitsos, D.E., Reid, P.C., Lavender, S.J., Edwards, M., Richardson, A.J., 2005. Extending the SeaWiFS chlorophyll data set back 50 years in the northeast Atlantic. Geophysical Research Letters 32, L06603. doi:10.1029/2005GL022484.
Rayner, N.A., Parker, D.E., Horton, E.B., Folland, C.K., Alexander, L.V., Rowell, D.P., Kent, E.C., Kaplan, A., 2003. Global analyses of sea surface temperature sea ice and night marine air temperature since the late nineteenth century. Journal of Geophysical Research 108 (D14), 4407. doi:10.1029/2002JD002670.
Reid, P.C., Edwards, M., Hunt, H.G., Warner, A.J., 1998. Phytoplankton change in the North Atlantic. Nature 391, 546.
Roemmich, D., Gilson, J., Davis, R., Sutton, P., Wijffels, S., Riser, S., 2007. Decadal spinup of the South Pacific subtropical gyre. Journal of Physical Oceanography 37, 162–173.
Ryan, J.P., Ueki, I., Chao, Y., Zhang, H., Polito, P.S., Chavez, F.P., 2006. Western Pacific modulation of large phytoplankton blooms in the central and eastern equatorial Pacific. Journal of Geophysical Research 111, G02013. doi:10.1029/2005JG000084.
Saji, N.H., Goswami, B.N., Vinayachandran, P.N., Yamagata, T., 1999. A dipole mode in the tropical Indian Ocean. Nature 401, 360–363.
Santer, B.D., Wigley, T.M.L., Gleckler, P.J., Bonfils, C., Wehner, M.F., AchutaRao, K., Barnett, T.P., Boyle, J.S., Brüggemann, W., Fiorino, M., Gillett, N., Hansen, J.E., Jones, P.D., Klein, S.A., Meehl, G.A., Raper, S.C.B., Reynolds, R.W., Taylor, K.E., 2006. Forced and unforced ocean temperature changes in Atlantic and Pacific tropical cyclogenesis regions. Proceedings of the National Academy Sciences USA 103, 13905–13910.
Sarmiento, J.L., Slater, R., Barber, R., Bopp, L., Doney, S.C., Hirst, A.C., Kleypas, J., Matear, R., Mikolajewicz, U., Monfray, P., Soldatov, V., Spall, S.A., Stouffer, R., 2004. Response of ocean ecosystems to climate warming. Global Biogeochemical Cycles 18, GB3003. doi:10.1029/2003GB002134.
Schneider, B., Bopp, L., Gehlen, M., Segschneider, J., Frölicher, T.L., Cadule, P., Friedlingdtein, P., Doney, S.C., Behrenfeld, M.J., Joos, F., 2008. Climate-induced interannual variability of marine primary and export production in three global coupled climate carbon cycle models. Biogeosciences 5, 597–614.
Sen, P.K., 1968. Estimates of the regression coefficient based on Kendall's tau. Journal of American Statistical Association 63, 1379–1389.
Shiskin, J., Young, A.H., Musgrave, J.C., 1967. The X-11 variant of the Census Method II seasonal adjustment program. Bureau of the Census, Technical Paper No. 15, 66 pp.
Signorini, S.R., Murtugudde, R.G., McClain, C.R., Christian, J.R., Picaut, J., Busalacchi, A.J., 1999. Biological and physical signatures in the tropical and subtropical Atlantic. Journal of Geophysical Research 104, 18367–18382.
Stenseth, N.C., Mysterud, A., Ottersen, G., Hurrell, J.W., Chan, K.-S., Lima, M., 2002. Ecological effects of climate fluctuations. Science 297, 1292–1295.
Stenseth, N.C., Ottersen, G., Hurrell, J.W., Mysterud, A., Lima, M., Chan, K.-S., Yoccoz, N.G., Ådlandsvik, B., 2003. Studying climate effects on ecology through the use of climate indices: The North Atlantic Oscillation, El Niño Southern Oscillation and beyond. Proceedings of the Royal Society of London, B 270, 2087–2096.
Sutton, P.J.H., Bowen, M., Roemmich, D., 2005. Decadal temperature changes in the Tasman Sea. New Zealand Journal of Marine and Freshwater Research 39, 1321–1329.
Tilburg, C.E., Subrahmanyam, B., O'Brien, J.J., 2002. Ocean color variability in the Tasman Sea. Geophysical Research Letters 29, 1487. doi:10.1029/2001GL014071.
Vantrepotte, V., Mélin, F., 2009. Temporal variability of 10-year global SeaWiFS time-series of phytoplankton chlorophyll *a* concentration. ICES Journal of Marine Science 66, 1547–1556.
Vantrepotte, V., Mélin, F., 2010. Temporal variability in SeaWiFS derived apparent optical properties in European seas. Continental Shelf Research 30, 319–334.
Vinayachandran, P.N., Kurian, J., Neema, C.P., 2007. Indian Ocean response to anomalous conditions in 2006. Geophysical Research Letters 34, L15602. doi:10.1029/2007GL030194.
Wang, C., Kucharski, F., Barimalala, R., Bracco, A., 2009. Teleconnections of the tropical Atlantic to the tropical Indian and Pacific Oceans: a review of recent findings. Meteorologische Zeitschrift 18, 445–454.
Wolter, K., Timlin, M.S., 1998. Measuring the strength of ENSO events—how does 1997/98 rank? Weather 53, 315–324.
Wong, S., Dessler, A.E., Mahowald, N., Colarco, P.R., da Silva, A., 2008. Long-term variability in Saharan dust transport and its link to North Atlantic sea surface temperature. Geophysical Research Letters 35, L07812. doi:10.1029/2007GL032297.